

# Dispersive modeling of breaking waves on a slope

Jihwan Kim<sup>a</sup>, Geir K. Pedersen<sup>a</sup>, Finn Løvholt<sup>a,b</sup>, Randall J. LeVeque<sup>c</sup>

<sup>a</sup>*University of Oslo, Department of Mathematics, Oslo, Norway*

<sup>b</sup>*Norwegian Geotechnical Institute, Oslo, Norway*

<sup>c</sup>*University of Washington, Department of Applied Mathematics, Seattle, USA*

---

## Abstract

The nonlinear shallow water model is widely used in the study of tsunami propagations, but an increasing number of studies are dedicated to the dispersion dynamics of tsunamis. If the wave dispersion becomes important, Boussinesq-type models are often used. In this work, an operational Boussinesq solver, *BoussClaw*, is introduced for modeling fully non-linear dispersive tsunami propagation, taking into account inundation. In the BOUSSCLAW model, Boussinesq equations from the literatures, based on the depth-averaged velocity and with enhanced dispersion properties, are implemented using a hybrid of the finite volume and finite difference methods. In order to validate BOUSSCLAW, numerical results are compared to the analytical solutions and laboratory experiments. Furthermore, the wave steepening and breaking motion is carefully scrutinized, and we demonstrate that the point of wave breaking may be wrongly identified in many of the commonly used Boussinesq models.

*Keywords:* Breaking wave, Boussinesq equation, finite volume method

---

## 1. Introduction

Tsunamis are often considered as long waves compared to the water depth, and long-wave models are consequently widely used in the study of their propagation and inundation. Through the use of numerical shock capturing techniques  
5 for modeling the nearshore bore formation of the tsunami, *nonlinear shallow water* (NLSW) models did become the standard model for modeling tsunami

propagation and run-up, see e.g. (Titov and Synolakis, 1995; Imamura, 1996; Harig et al., 2008; Berger et al., 2011).

The NLSW models do not incorporate frequency dispersion, which may be  
10 included by ascending in the hierarchy of long wave expansion to the Boussinesq  
type equations. Numerical models based on Boussinesq type equations have  
been used for idealized studies of wave processes since 1966 (Peregrine, 1966) and  
additionally to simpler problems in coastal engineering in the following decades  
(Brocchini, 2013). However, the accumulated effect of the frequency dispersion  
15 for the wave propagation over the open sea is a function of propagation time  
and the shape of the disturbance (Glimsdal et al., 2013), and may become  
important for some tsunamis, in particular for landslide sources (Løvholt et al.,  
2015). Dispersion may further be of importance, in combination with non-  
linear effects, for the evolution of undular bores for tsunamis (Glimsdal et al.,  
20 2013; Grue et al., 2008; Løvholt et al., 2008; Behrens and Dias, 2015). In  
the last decades we have seen a development on long wave expansions and  
their numerical formulations. In the 1990s the modeling with Boussinesq type  
equations were vitalized by new formulations, in particular those of Madsen  
and Sørensen (1992) and Nwogu (1993) which displayed improved dispersion  
25 properties in comparison to the standard formulation of Peregrine (1967). **A  
few more lines here**

In their original formulation, Boussinesq-type models do not take into ac-  
count the post-breaking motion. In order to combine breaking with the Boussinesq-  
type equations several strategies have therefore been suggested. For instance,  
30 Peregrine (1967) used  $A/h = 0.6$  as the break threshold, while pointing out that  
this value could reach around 2 in laboratory experiments. Another way of in-  
corporating the breaking that was suggested by Kennedy et al. (2000) included  
diffusive terms in the momentum equation to smear out sharp fronts. Løvholt  
et al. (2013) similarly employed a diffusive model including transport terms,  
35 but pointed out that breaking wave Boussinesq models were prone to instabili-  
ties. Schäffer et al. (1993) introduced the concept of the *surface roller*. Lynett  
(2006) investigated  $\eta_t/c$ ,  $\eta_x$ ,  $u_{xx}H^2/c$ , and  $u/c$ , where  $c = \sqrt{gH}$ ,  $u$  is the wave

speed and  $\eta$  is the water surface elevation, and then identified that the critical front slope ( $\eta_x$ ) is the least sensitive breaking threshold. Tissier et al. (2012) suggested a breaking decision model based on the surface roller, the maximal front angle and the Froude number. An alternative non-linear diffusive ad-hoc breaking term was suggested Matsuyama et al. (2007), based on their large scale experiments of the wave propagation of undular bores on various slope angles.

Recent developments of operational Boussinesq models, have made use of more sophisticated hybrid numerical techniques such as use of approximate Riemann solvers combined with TVD limiters for the conserved variables, and finite differences for additional higher order terms (Erduran et al., 2005; Kim et al., 2009; Shi et al., 2012), leading among others to the popular FUNWAVE-TVD and COULWAVE-TVD applications. For instance in Shi et al. (2012), Boussinesq terms are switched off the near-shore region where large amplitude-to-depth-ratios occur, implying that only NLSW terms remain in the shallowest region. This allows for a relatively robust treatment of the modeling of the post breaking phase. To this end, the  $A/h = 0.8$  threshold suggested by (Shi et al., 2012) based on the Froude similarity analysis by Tonelli and Petti (2009), have in many ways become the standard for incorporating breaking in a feasible and practical way.

In this paper, we present a new hybrid Boussinesq type model BOUSSCLAW, of similar mould as FUNWAVE-TVD and COULWAVE-TVD. The emphasis is twofold. First, to present a careful validation of the model, both towards laboratory experiments and more general reference models. Second, we use the new model in comparison with a full potential reference model to explore how accurate the Boussinesq models can represent the wave evolution until the point of breaking. In the present example, we are finally able to demonstrate that Boussinesq models may be employed to accurately model the near shore tsunami propagation beyond the standard  $A/h = 0.8$  threshold depth. Conversely, we find that the use of the standard  $A/h = 0.8$  threshold depth invokes a too early formation of a breaking bore. This points out that that the breaking criteria employed so far lacks generality.

This paper is organized as follows: In Section 2, the base model for the  
70 wave equations is given and the numerical scheme is outlined, including a von  
Neuman stability analysis. Sections 3 compares results from the BOUSSCLAW  
with the analytic solutions and laboratory experiments. Section 4 discusses the  
wave steepening and using a Boundary Integral Method (BIM) for solving the  
full potential equations. In Section 5, we compare these results of pre-breaking  
75 evolution with Boussinesq type models.

## 2. Model Description

Boussinesq-type equations include non-hydrostatic pressure in an approxi-  
mate way treat short waves more accurately than the shallow water equations.  
The Boussinesq-type wave models have been derived on the assumption that  
80  $\mathcal{O}(\epsilon)$  and  $\mathcal{O}(\mu)$  terms are small, where  $\epsilon$  and  $\mu$  denote the ratio of wave am-  
plitude to depth and the ratio of depth to wavelength respectively. Various  
models have been suggested, and the papers of Peregrine (1967), Madsen and  
Sørensen (1992), Nwogu (1993), Lynett et al. (2002), and Wei and Kirby (1995)  
are representative examples.

85 In this work, a new numerical model, called BOUSSCLAW, is introduced. It is  
an extension of GEOCLAW Clawpack Development Team (2016), and solves the  
Boussinesq-type equations derived by Schäffer et al. (1993). The BOUSSCLAW  
model is a hybrid of the finite volume and finite difference solvers with the  
operation splitting technique. The GEOCLAW software is a part of Clawpack  
90 Development Team (2016) developed mainly by by LeVeque (1997), George  
(2008) and Berger et al. (2011) which is designed to solve the nonlinear shallow  
water equations.

### 2.1. BOUSSCLAW - a new long wave model for tsunami propagation and run-up

#### 2.1.1. Boussinesq-type equations

Schäffer et al. (1993) derived Boussinesq-type equations with an addition of

a Padé approximation of the linear dispersion relation. The equations read

$$H_t + (Hu)_x = 0, \quad (1)$$

$$(1 - D)[(Hu)_t] + \left(Hu^2 + \frac{g}{2}H^2\right)_x - gHh_x - Bgh^2(h\eta_x)_{xx} = 0, \quad (2)$$

where the operator  $D$  is defined as

$$D(w) = \left(B + \frac{1}{2}\right)h^2w_{xx} - \frac{1}{6}h^3\left(\frac{w}{h}\right)_{xx}, \quad (3)$$

95 for any  $w(x, t)$ . In the above equations  $H(x, t)$  and  $u(x, t)$  are the total flow depth and the depth averaged velocity of the water, respectively,  $h(x)$  is the still water depth,  $\eta(x, t)$  is the surface elevation, and thus  $H(x, t) = h(x) + \eta(x, t)$ . Moreover,  $g$  is the acceleration of gravity, and  $B$  is a dispersion parameter. Madsen and Sørensen (1992) has chosen the parameter  $B = 1/15$  from a Padé expansion of the linear dispersion analysis. When  $B = 0$ , this set of the Boussinesq-  
100 type equations approximately reduces to that of Peregrine (1967) as the linear dispersion relations are identical. However, unlike Peregrine's momentum equation the hydrostatic parts of (2) are written in a conservative form. Moreover, some nonlinearity is introduced in the dispersion term for convenience. Even  
105 though (1), (2) and (3) do not constitute a fully nonlinear set of Boussinesq, they do describe shoaling of solitary waves markedly better than, for instance, Peregrine equations, as will be demonstrated in section 5.

The BOUSSCLAW model solves the Boussinesq-type equations (1) and (2) numerically with a hybrid combination of the finite volume and finite difference  
110 methods that will be explained in a moment. There have been several studies on this type of hybrid schemes. For example, see Tissier et al. (2011), Shi et al. (2012) and Dutykh et al. (2013).

To facilitate a fractional step method, as outlined below, we move the hydrostatic terms of (2) inside the  $(1 - D)$  operator, while balancing with extra terms in the  $\Psi$ , to obtain

$$(1 - D)[(Hu)_t] + \left(Hu^2 + \frac{g}{2}H^2\right)_x - gHh_x = -\Psi(x, t), \quad (4)$$

where

$$\begin{aligned} \Psi(x, t) = & \left( B + \frac{1}{2} \right) h^2 \left( (Hu^2)_x + gH\eta_x \right)_{xx} \\ & - \frac{1}{6} h^3 \left( \frac{(Hu^2)_x + gH\eta_x}{h} \right)_{xx} - Bgh^2 (h\eta_x)_{xx}. \end{aligned} \quad (5)$$

### 2.1.2. Numerical scheme

The equations (1) and (4) are written in a form that conserves momentum to leading order in  $\mu$ , but with the  $\Psi$  term as a pseudo source. Such equations may be solved by a *fractional step method* as described in LeVeque (2002), for instance. First, it is observed that (4) may be formally rewritten as

$$(Hu)_t = - \left\{ \left( Hu^2 + \frac{g}{2} H^2 \right)_x - gHh_x \right\} - (1 - D)^{-1} \Psi(x, t), \quad (6)$$

At the first stage of the hybrid scheme, we integrate  $Hu$  over a time step taking into account all hydrostatic terms, namely those within the braces on the right hand side, and omitting the source terms involving  $\Psi$ . When this is combined with the continuity equation (1) this simply corresponds to advancing the shallow water equations one time step forward. To this end we employ GEOCLAW, a high-order accurate finite volume solver for the shallow water equations with adaptive mesh refinements.

In the second stage, we retain the new  $H$  value, but integrate  $Hu$  (essentially being the momentum density) further from the first stage by solving

$$(1 - D) [(Hu)_t] = -\Psi. \quad (7)$$

Since the differential operator  $D$  contains spatial derivatives, a systems of difference equations must then be solved.

The spatial and time discretization should be carefully chosen for the stability of the second stage. In our numerical scheme, the second order centered scheme is used for the spatial discretization, and a four stage Runge-Kutta method is used for the time integration. The von Neumann stability analysis of this numerical scheme is outlined in Appendix A.

Suppose the spatial domain is divided into  $n$  grid cells with the spatial grid size  $\Delta x$ . Arrays of nodal values for flow depth and  $Hu$ , respectively, are defined as

$$\mathbf{H} = (H_1, H_2, \dots, H_n)^T,$$

$$\mathbf{M} = (H_1 u_1, H_2 u_2, \dots, H_n u_n)^T.$$

With time increment  $\Delta t$  the fourth order Runge-Kutta scheme can be written as follows,

$$\mathbf{M}^1 = \mathbf{M}, \quad \mathbf{M}^2 = \mathbf{M} + \frac{\Delta t}{2} \mathbf{S}^1, \quad \mathbf{M}^3 = \mathbf{M} + \frac{\Delta t}{2} \mathbf{S}^2, \quad \mathbf{M}^4 = \mathbf{M} + \Delta t \mathbf{S}^3, \quad (8)$$

where  $\mathbf{M}^k$  are intermediate value arrays and  $\mathbf{S}^k$  are correspondingly arrays for the time derivatives of  $Hu$ , obtained by solving

$$(I - \bar{D})\mathbf{S}^k = -\bar{\Psi}(\mathbf{H}, \mathbf{M}^k), \quad \text{for } k = 1, \dots, 4. \quad (9)$$

Here  $\bar{\Psi}$  and  $\bar{D}$  represent centered spatial discretizations for the term  $\Psi$  and the operator  $D$ , respectively. These are given explitley below. Finally the value of  $\mathbf{M}$  at the new time level is obtained by

$$\mathbf{M}^+ = \mathbf{M} + \frac{\Delta t}{6} [\mathbf{S}^1 + 2\mathbf{S}^2 + 2\mathbf{S}^3 + \mathbf{S}^4]. \quad (10)$$

In (9),  $\bar{D}$  is a tri-diagonal  $n \times n$  matrix with elements

$$\bar{D}_{i,i-1} = \frac{1}{\Delta x^2} \left[ \left( B + \frac{1}{2} \right) h_i^2 - \frac{1}{6} \frac{h_i^3}{h_{i-1}} \right],$$

$$\bar{D}_{i,i} = \frac{1}{\Delta x^2} \left( -2B - \frac{2}{3} \right) h_i^2,$$

$$\bar{D}_{i,i+1} = \frac{1}{\Delta x^2} \left[ \left( B + \frac{1}{2} \right) h_i^2 - \frac{1}{6} \frac{h_i^3}{h_{i+1}} \right].$$

Correspondingly, the  $i$ -th element of  $\Psi(\bar{\mathbf{H}}, \mathbf{q})$  is

$$\begin{aligned}\bar{\Psi}_i = & \left( B + \frac{1}{2} \right) \frac{h_i^2}{2\Delta x^3} \left[ \left( \frac{M_{i+2}^2}{H_{i+2}} - 2\frac{M_{i+1}^2}{H_{i+1}} + 2\frac{M_{i-1}^2}{H_{i-1}} - \frac{M_{i-2}^2}{H_{i-2}} \right) \right. \\ & \left. + g(H_{i+1}(\eta_{i+2} - \eta_i) - 2H_i(\eta_{i+1} - \eta_{i-1}) + H_{i-1}(\eta_i - \eta_{i-2})) \right] \\ & - \frac{1}{6} \frac{h_i^3}{2\Delta x^3} \left[ \frac{M_{i+2}^2/H_{i+2} - M_i^2/H_i}{H_{i+1}} - 2\frac{M_{i+1}^2/H_{i+1} - M_{i-1}^2/H_{i-1}}{h_i} \right. \\ & \left. + \frac{M_i^2/H_i - M_{i-2}^2/H_{i-2}}{H_{i-1}} \right. \\ & \left. + g \left( \frac{H_{i+1}(\eta_{i+2} - \eta_i)}{H_{i+1}} - 2\frac{H_i(\eta_{i+1} - \eta_{i-1})}{h_i} + \frac{H_{i-1}(\eta_i - \eta_{i-2})}{H_{i-1}} \right) \right] \\ & - \frac{Bgh_i^2}{2\Delta x^3} (H_{i+1}(\eta_{i+2} - \eta_i) - 2H_i(\eta_{i+1} - \eta_{i-1}) + H_{i-1}(\eta_i - \eta_{i-2})),\end{aligned}$$

for  $i = 1, 2, \dots, n$ .

## 2.2. Models for comparison

130 The performance of the Boussinesq model presented here is assessed by comparison with numerical results from a full potential flow model which is described in Løvholt et al. (2013) and references therein. The model is based on a boundary integral technique and is run with fully nonlinear solitary wave solutions as initial conditions. During shoaling and breaking this model can describe  
135 the evolution of a plunger, but breaks down when the plunger reaches the free surface. Hence, the potential flow results are used to determine the point of breaking due to shoaling and to evaluate the evolution of amplitude and wave shape of the current model until this point. Below we refer to the full potential model as the BIM (Boundary Integral Method) model.

140 Comparison with a pre-existing, fully nonlinear Boussinesq model is facilitated by the application of a Lagrangian model, described in Løvholt et al. (2013). Apart from the use of Lagrangian coordinates the equations employed in this model are similar to (1) and (2). They differ only concerning the nonlinearities in the dispersion terms and that the dispersion optimization terms  
145 are added in a fully nonlinear fashion. Presently, the Lagrangian model has



no established bore capturing facility and is hence valid only to the point of breaking. Results from this model will be referred to as 'Serre', even though the dispersion enhancement is invoked.

Results for the Peregrine-type Boussinesq equations are obtained by the  
150 GloBouss model. This is a dispersive tsunami propagation model which is based on Peregrine-type equations and discretization on a staggered grid. Further details are found in Løvholt et al. (2008).

For comparison also the version 2.1 of the FUNWAVE-TVD model by Shi  
et al. (2012) is used. The FUNWAVE-TVD model shares important features  
155 with BOUSSCLAW, employing a hybrid of the finite volume and finite difference scheme to solve the fully non-linear higher order dispersive Boussinesq model numerically. While we refer to Shi et al. (2012) for details, we briefly note that FUNWAVE-TVD is based the fully nonlinear Boussinesq equations of Chen (2006). The numerical spatial representation in FUNWAVE-TVD is MUSCL  
160 TVD scheme to discretize for the flux and first order terms, whereas a central finite difference scheme Wei et al. (1995) is utilized for the higher order momentum terms. A Runge-Kutta scheme is employed for the time stepping.

### 3. Numerical Tests

#### 3.1. Solitary wave propagation

In order to validate the numerical approach a solitary wave propagation is tested on a constant water depth. For the initial conditions, the analytic solitary wave solution of the Serre's equations is used since analytic solutions are unknown for the set (1) and (2). Solitary wave solutions to Serre's equations are given as

$$\begin{aligned}\eta(x, t) &= A \operatorname{sech}^2(\kappa(x - ct)), \\ u(x, t) &= c \frac{\eta(x, t)}{h},\end{aligned}\tag{11}$$

where

$$\kappa = \frac{\sqrt{3h}}{2A\sqrt{A+h}}, \quad \text{and} \quad c = \sqrt{g(A+h)}.\tag{12}$$

165 In this expression,  $A$  and  $h$  are constants which represent the wave amplitude and the undisturbed water depth respectively.

In Figure 1, snapshots from the BOUSSCLAW's simulation are shown at  $t = 0, 4, 8$  and  $12$  with  $\Delta x = 0.1$ . For the initial conditions, the solution (11) is used with  $A = 0.2$ ,  $h = 1$  and  $g = 9.81$ . The computational results are in good  
 170 agreement with the analytic solutions concerning height, shape and propagation speed. The amplitudes decreases very gently as the wave propagates.

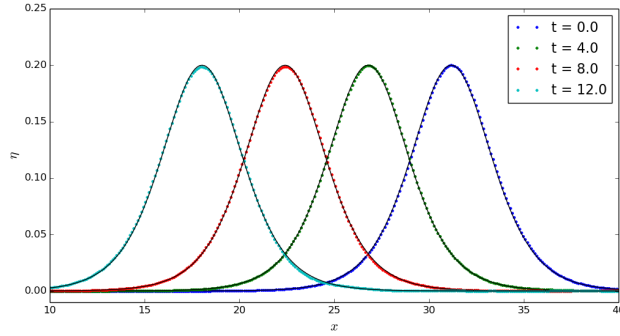


Figure 1: Snapshot of the analytic and computed solitary wave at  $t = 0, 4, 8$  and  $12$  with  $A/h = 0.2$ . The wave propagates from right to left, and the analytic solutions are black solid lines.

The wave energies for the shallow water equations and the Boussinesq equations are  $E_0$  and  $E_0 + E_1$ , respectively, where

$$E_0 = \frac{1}{2} (g\eta^2 + H\bar{u}^2), \quad (13)$$

$$E_1 = \frac{1}{6} H^3 \bar{u}_x^2 + \frac{1}{2} H^2 h_x \bar{u} \bar{u}_x + \frac{1}{2} H h_x^2 \bar{u}^2. \quad (14)$$

Details are given in (Madsen et al., 1997) and Appendix B.

In Figure 2a, the energy of the solitary wave is shown with  $A/h = 0.2$  and  $\Delta x = 0.2$ . There are fluctuations both in the potential and kinetic energy that is evident when we zoom in, and the total energy decreases showing that the numerical procedure has dissipation. In Figure 2b, the relative error of the

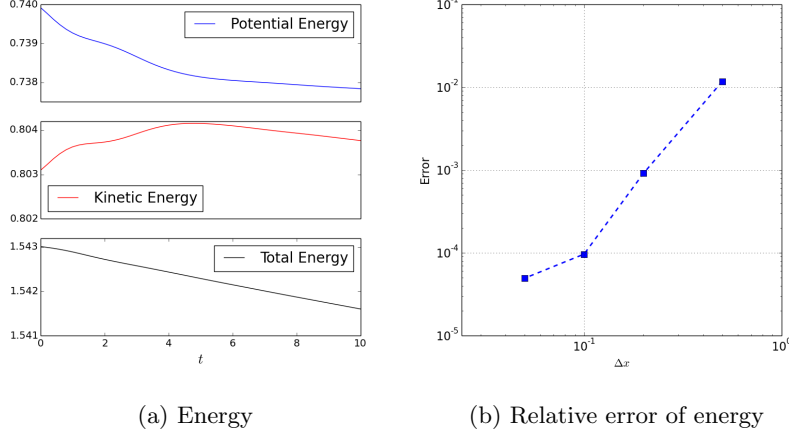


Figure 2: The energy of a solitary wave with  $\Delta x = 0.2$  (left), and log-log plot of relative error at  $t = 10$  for  $\Delta x = 0.05, 0.1, 0.2$  and  $0.5$  (right).

energy at  $t = 10$ ,

$$Error = \frac{|E_{t=0} - E_{t=10}|}{|E_{t=0}|},$$

is shown for different  $\Delta x$ . For a solitary wave on a constant depth, the energy dissipation decreases with the grid increments.

### 3.2. Waves on a composite slope

A physical model was constructed at the Coastal Hydraulic Laboratory of the U.S. Army Corps of Engineers in order to address beach erosion and severe flooding problems Briggs et al. (1995). The model beach consists of three piece-wise linear slopes of 1:53, 1:150, and 1:13 with a vertical wall at the shoreline as shown in Figure 3. In the laboratory, the wavemaker was located at 23.23 m. The gauge data from three cases are provided where the ratio  $A/h$  is equal to 0.038, 0.259 and 0.681 with  $h = 21.8$  cm.

The second case with  $A/h = 0.259$  has been compared with the numerical tests which employed 400 grid points. To specify the incoming wave from the left boundary, the data at Gauge 4 were used for the wave height, and the corresponding velocity (11) was applied.

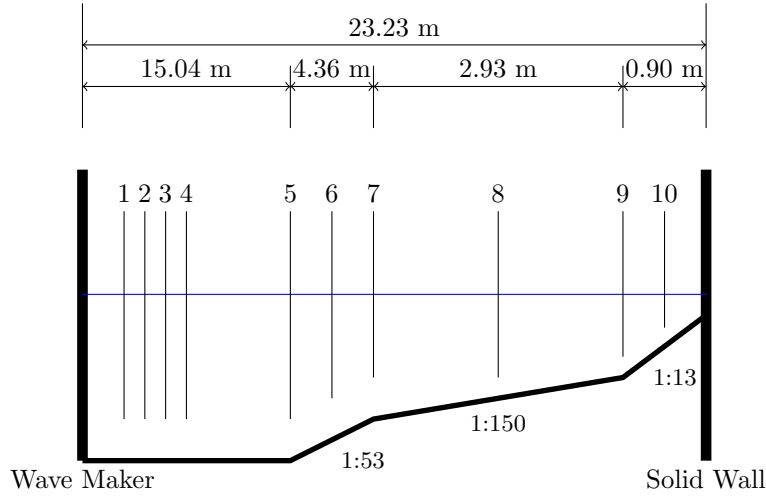


Figure 3: A sketch of the water tank

In Figure 4, water surface elevations at gauges 5, 7 and 8 are shown. The simulated waves are in good agreement with the laboratory measurements. For the reflected waves, larger discrepancies are observed. The increased discrepancy occurs because the full interaction between the wave and the wall at the right boundary is less accurately captured. Friction forces influence the wave evolution along the shallow region near the right wall, but we have not included these in the present numerical simulation. A better fit may possibly be obtained by incorporating friction, however, tuning the friction models is not the scope of this work.

#### 4. Simulation of wave steepening and breaking using a BIM model

Synolakis (1987) performed a series of laboratory experiments for the run-up of solitary waves on uniform slopes. Here, we are interested in the breaking cases. One such example in Synolakis (1987) is a solitary wave of amplitude  $A/h = 0.28$  approaching a slope of 1 : 19.85. In Figure 5, the initial set-up for a test is shown.

The set-up of the wave tank in the simulations follows the laboratory experiments by Synolakis (1987). The bathymetry of the wave tank is composed of a

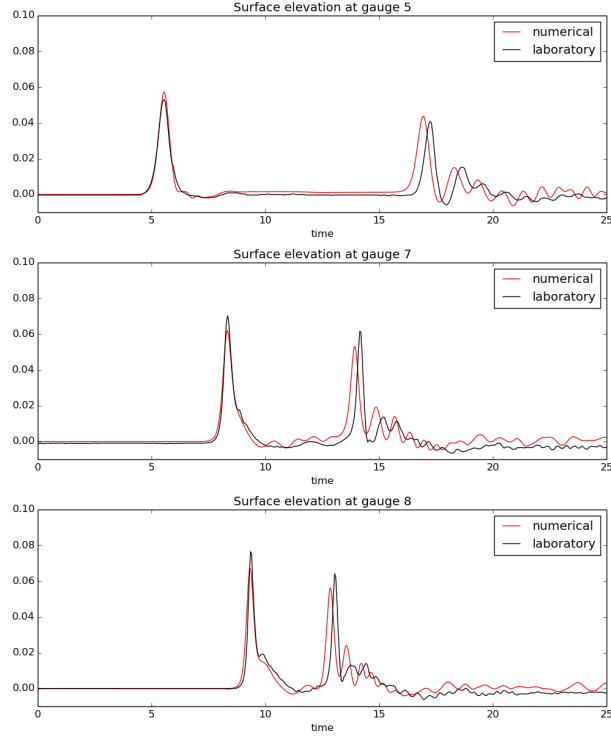


Figure 4: Water surface elevation at gauges 5,7 and 8 for  $A/h = 0.269$  case.

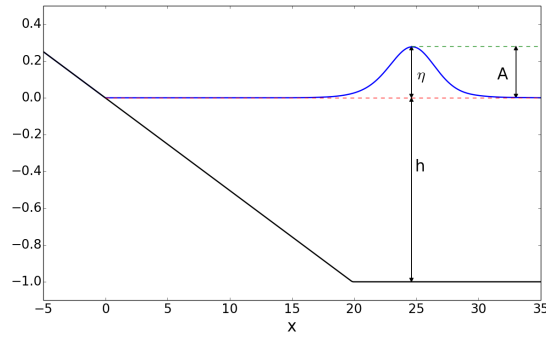


Figure 5: Set-up of a numerical test for Synolakis' experiments.

horizontal bottom and a uniform slope as shown in Figure 5. A solitary wave of  
 205 amplitude  $A/h = 0.28$  is generated at the right end of the tank and propagates  
 leftwards to the beach.

We present the results using the non-dimensional time  $t^* = t\sqrt{h/g}$  and non-dimensional space  $x^* = x/h$ . In the following, we drop the asterisks in the presentation of the results. In Synolakis (1987),  $t = 0$  was defined as when the wave crest was a non-dimensional distance,  $L$ , from the toe of the slope, where

$$L = \sqrt{\frac{4A}{3h}} \operatorname{arccosh} \left( \frac{1}{0.05} \right).$$

However, at  $t = 0$ , the solitary wave has an elevation of 5% of its maximum at the toe of the beach, meaning that the slope has started to interact with the solitary wave. To avoid any such interaction obscuring our analysis, we instead place the  
210 initial solitary wave using equation (11) at  $L + 5c$ , where  $c$  is the shallow water wave celerity. In this way, the initial solitary wave has a negligible interaction with the slope when initialized.

In Figure 6, the laboratory measurements are shown with the computational results from the BIM model for a breaking wave case of Synolakis with  $A/h =$   
215 0.28 and 1 : 19.85 slope at  $t = 15$ .

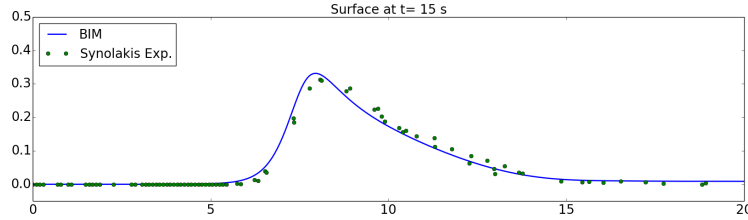


Figure 6: Comparison of the laboratory experiments and BIM at  $t=15$  with  $A/h = 0.28$  on a slope of 1 : 19.85.

Figure ?? shows the numerical results from the BIM model at  $t = 17, 18$  and 18.6. In the BIM results a vertical front is observed at  $x = 4.02$  and  $t = 18.6$  with the maximum wave amplitude  $A = 0.414$ , and this shows similarity with the analysis of Titov and Synolakis (1995) on the wave breaking point. The ratio  
220 of amplitude to depth,  $A/h$ , is about 2.01 at the break point. The potential flow model cannot be run much beyond the breaking points (until the attachment of the plunger only) and gives no information on the following bore propagation. In Figure ??, computations of the shallow water equations (present model without

the second fractional step) display a premature bore formation which checks the  
225 amplification during the subsequent shoaling. As a consequence the amplitude  
in the shallow water equations simulation is markedly smaller than that of the  
potential flow model when the latter indicates breaking.

## 5. Pre-breaking and breaking wave evolution using depth averaged models

230 We use the set-up described in section 4 for the Boussinesq modeling of  
solitary waves on a slope. Figure ?? shows the snapshots of the water surface  
at  $t=16$  and  $18.6$  from BIM and BOUSSCLAW with  $B=0$  and  $1/15$ . When the  
wave is smooth at  $t=16$ , the BOUSSCLAW results are similar. At the breaking  
point,  $t = 18.6$ , larger differences are observed. If  $B = 0$ , the wave speed is  
235 slightly faster than the BIM result, but the wave amplitude is similar. When  
 $B = 1/15$ , the wave speed matches the BIM results better, but the amplitude  
is slightly smaller. In general, the computational results are rather similar with  
 $B = 0$  and  $1/15$ .

Next, the BOUSSCLAW simulations are compared with those of other Boussi-  
240 nesq solvers, namely FUNWAVE (Shi et al., 2012), GLOBOUSS (Løvholt et al.,  
2010) and the Serre type formulation (Løvholt et al., 2013). As noted above,  
the original Serre’s equations are enhanced by adding the Schäffer et al. (1993)  
terms.

In Figure 7, snapshots from different numerical models are shown at  $t=16$ ,  $18$   
245 and  $20$ . At  $t=16$ , the computational results from the Boussinesq-type equations  
show similar results. At  $t=18$ , some discrepancies are observed that can be split  
into two groups, and GLOBOUSS and FUNWAVE are similar while BOUSSCLAW  
and Serre’s results are similar. The wave amplitudes computed by GLOBOUSS  
and FUNWAVE, are more than 10 % larger than BIM. The wave amplitude  
250 continues to increase with GLOBOUSS simulations, and the difference from the  
BOUSSCLAW result becomes larger at  $t = 20$ . The results from the Serre and  
BOUSSCLAW models clearly more similar to those of the BIM model. Especially,

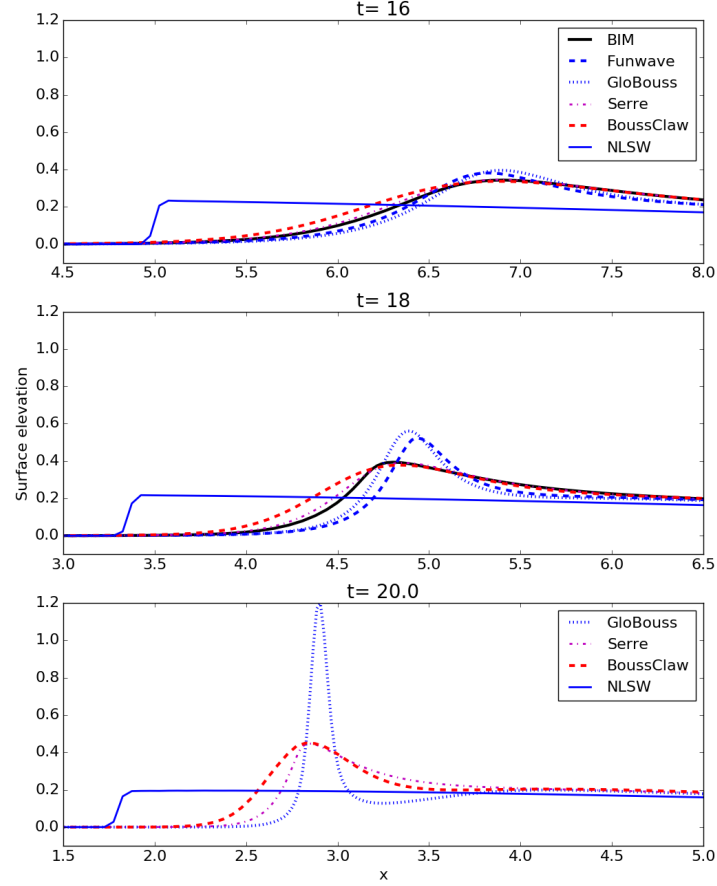


Figure 7: Snapshots of BIM, Serre, GLOBOUSS, BOUSSCLAW and FUNWAVE at  $t = 16$ , 18 and 20. The BOUSSCLAW is used with  $B=1/15$ , and the Peregrine's form is used for GLOBOUSS.

the wave amplitudes are correctly determined by these models.

### 5.1. Wave breaking and run-up

255 In order to catch wave breaking in a heuristic fashion, we may choose to invoke the threshold  $\epsilon_B := \eta/h$  for BOUSSCLAW. When the threshold is reached, the wave breaking is supposed to be initiated, and the dispersive terms are



suppressed. At the breaking, the set of equations is locally switched to the shallow water equations for the corresponding wave packet, and the trailing waves are solved with the Boussinesq equations if the thresholds are not reached. In the numerical simulation of the BOUSSCLAW model, the ratio  $\epsilon_B$  reaches the threshold 0.8 at  $t = 14.9$  when the peak of the wave is at  $x = 8.03227$ . In the following, we explore the wave evolution with and without the application of this threshold.

When a wave reaches the coastline, the coastline changes in time as the wave runs up the slope and recedes eventually. For the numerical simulations, it has been a challenge to compute the inundation correctly. At the coastline, the BOUSSCLAW use the GEOCLAW software which can handle wet and dry states with the depth positivity property. Details can be found at George (2008).

Friction terms are necessary in the numerical simulations to capture the inundation appropriately. For example, the Figure 8 shows that the run-up height is larger than the experiments without the friction terms. BOUSSCLAW uses the Manning-type frictions as follows,

$$f_D = -\frac{gC_d^2 u|u|}{H^{5/3}},$$

where  $C_d$  is a Manning drag coefficient. Another parameter  $d^*$  needs to be chosen so that the water depth is set as  $H = 0$  if the water depth is smaller than this threshold,  $H < d^*$ . Antuono et al. (2012) derived an approximate solution of the shoreline for the shallow water equations with the Chezy friction, and studied the effect of the frictional coefficient and the water depth tolerance. In this work, the parameter  $d^*$  is set as  $10^{-4}$ .

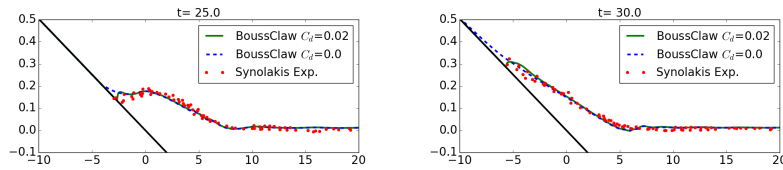


Figure 8: Comparison of experiments and BoussClaw results at  $t=25$  and  $30$ .

In Figure 9, snapshots are shown at  $t=20$ ,  $25$ , and  $30$  from BOUSSCLAW and

NLSW with friction forces  $C_d = 0.02$ . We compared the NLSW and BOUSS-  
 CLAW with  $\epsilon_B = 0.8$  and without the threshold. At  $t=20$ , the difference in the  
 wave height is clearly observed. With  $\epsilon_B = 0.8$ , the governing equations have  
 280 already switched to NLSW, and the bore is formed at the front. At  $t=25$  and  
 30, the wave is running up the slope, and the difference in the run-up height  
 is relatively small. At  $t=30$ , two BOUSSCLAW results are similar in the run-up  
 height, but small waves are observed around  $x = 7$  for the BoussClaw with  
 $\epsilon_B = 0.8$ .

285 Figure 10 shows the amplitude to depth ratio,  $\epsilon_B$ , as function of the crest  
 location. With BIM simulations, the wave starts breaking at  $x = 4.09$ . When  
 the crest in the BOUSSCLAW simulation reaches  $x = 4.09$  we find  $A/h = 1.97$ ,  
 the ratio of wave speed to celerity ( $u/\sqrt{gH}$ ) is 1.034 and maximum surface slope  
 angle of  $39.1^\circ$ .

## 290 5.2. Wave Energy

The wave energy is nearly conserved when the wave is smooth, but decreases  
 as the wave breaks. The wave energy expressions for the shallow water equations  
 and Boussinesq equations are  $E_0$  and  $E_0 + E_1$  respectively, which are given in  
 (13) and (14).

295 In Figure 11, the wave energy  $E_0$  and  $E_0 + E_1$  are shown. The energy  
 denotes the aggregate of the wave energy in the entire computational domain  
 and is shown as function of the crest location. In the left panel, the energy  
 $E_0$  is well-preserved for the shallow water equations before the wave forms a  
 shock, and then the energy dissipates after a shock is formed. In the right  
 300 panel,  $E_0 + E_1$  is well-preserved for the BOUSSCLAW simulation during deep  
 water propagation, but the value decreases slightly as the wave steepens near  
 the shoreline. When the threshold  $\epsilon_B = 0.8$  is used, the energy  $E_0 + E_1$  is well-  
 preserved as shown on the right figure before the threshold is reached. When  
 the crest is located at  $x = 8.03227$  with  $\epsilon_B = 0.8$ , the wave energy  $E_0$  on the left  
 305 figure does not decrease immediately. The energy  $E_0$  is preserved for a while,  
 then starts to decrease as a shock is formed.

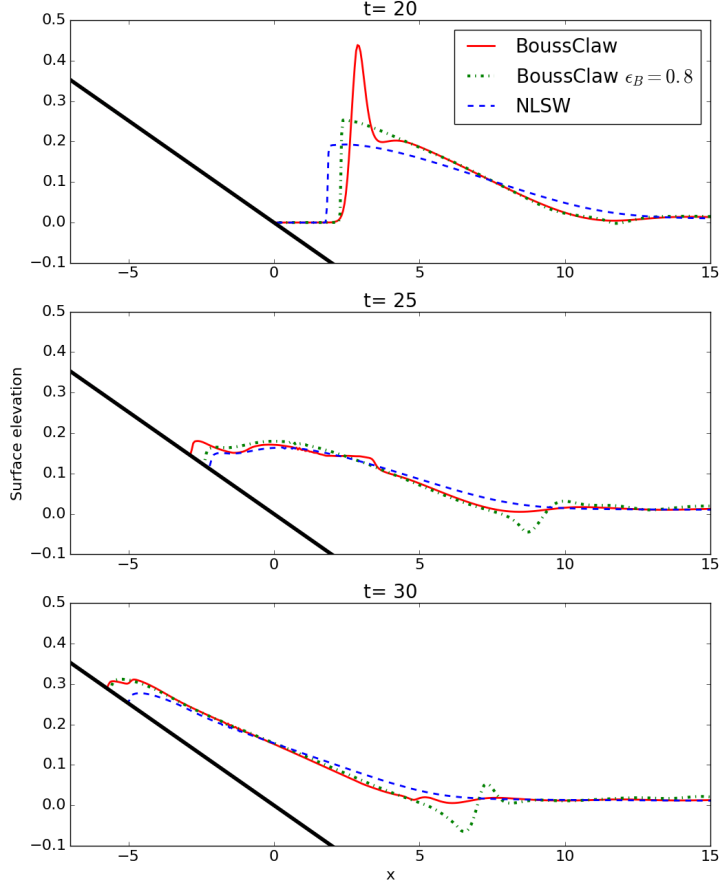


Figure 9: Comparison of BOUSSCLAW and NLSW with  $\epsilon_B = 0.8$  at  $t = 20, 25$  and  $30$ . Fiction forces have been added with  $C_d = 0.02$ .

## 6. Conclusion

In the present paper we have presented a new operational Boussinesq type model, BOUSSCLAW, for modeling fully non-linear dispersive tsunami propaga-  
 310 tion, taking also into account drying-wetting during inundation and withdrawal on the beach. BOUSSCLAW resembles much used operational models such as

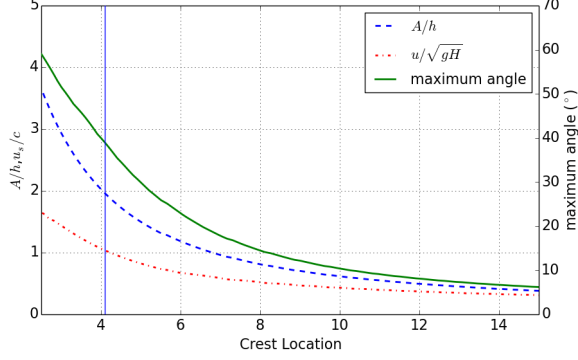


Figure 10: Plot of  $A/\eta$ ,  $u_s/c$  and maximum angle of waves vs. crest location. BIM shows the wave break at  $x = 4.09$ .

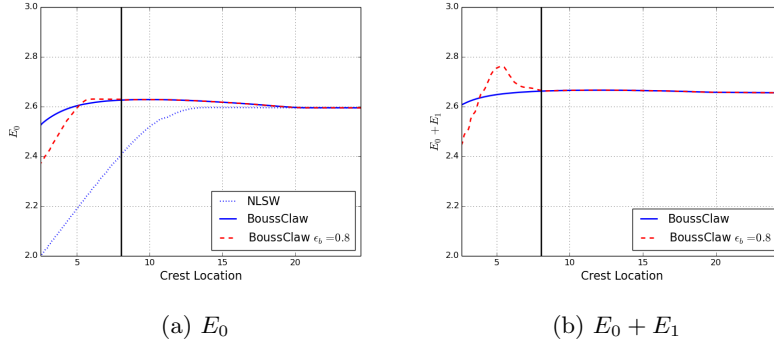


Figure 11: Energy plots of NLSW and BOUSSCLAW. The vertical line is at  $x = 8.03227$  m where  $\epsilon_B = 0.8$ , and the governing equations are switched to the NLSW from the Boussinesq equations.

FUNWAVE-TVD and COULWAVE-TVD, but is based on a slightly simpler and more transparent set of governing equations, and has a slightly different numerical scheme. We have tested numerical implementation towards analytical  
315 solitary wave expressions as well as laboratory experiments.

Making use of the experiments of Synolakis (1987) enabled us to constrain a set of different long wave models, including BOUSSCLAW, as well as a full potential BIM reference model. Using the BIM, we were able to explore in detail the post-breaking behaviour, and to identify the point of breaking accurately.

320 This was useful for determining the validity of the respective long wave models.  
 First, we found that by using standard NLSW models, the point of breaking  
 will be located too far offshore. Boussinesq models provide the opportunity  
 of providing a more accurate description of the near shore propagation and  
 shoaling. However, in current practise the Boussinesq terms are often omitted  
 325 near shore through the  $A/h > 0.8$  threshold criteria. As a consequence, the  
 point of breaking may be misinterpreted also in Boussinesq type models.

In the present example, we investigated the near shore propagation over  
 a relatively gentle shelf of  $1/19.85$  slope, and in this case the actual onset of  
 breaking occurred for  $A/h \approx 2$ , which is significantly later than what would be  
 330 predicted in any standard approach (NLSW or Boussinesq). As demonstrated  
 in this paper, the combined effects of non-linearities and dispersion influence the  
 solution markedly, when accumulated to the point of breaking. It is noted that  
 the artificial effect discovered would depend on the slope, and the  $A/h = 0.8$   
 limited may well work better on a much gentler slope as it is primarily derived  
 335 based on solitary wave evolution on constant depth. On the other hand,  $1/19.85$   
 slope is already quite gentle, and the offset between the reference solution and  
 Boussinesq models using this criteria may be even more pronounced for steeper  
 slopes.

## References

- 340 V. V. Titov, C. E. Synolakis, Modeling of breaking and nonbreaking long-wave  
 evolution and runup using VTCS-2, *Journal of Waterway, Port, Coastal, and  
 Ocean Engineering* 121 (6) (1995) 308–316.
- F. Imamura, Long-wave runup models, chapter Simulation of wave-packet prop-  
 agation along sloping beach by TUNAMI-code, *World Scientific* 3 (1996) 4.
- 345 S. Harig, Chaeroni, W. S. Pranowo, J. Behrens, Tsunami simulations on several  
 scales, *Ocean Dynamics* 58 (5) (2008) 429–440, ISSN 1616-7228.
- M. J. Berger, D. L. George, R. J. LeVeque, K. T. Mandli, The GeoClaw software

- for depth-averaged flows with adaptive refinement, *Adv. Water Res.* 34 (2011) 1195–1206.
- 350 D. H. Peregrine, Calculations of the development of an undular bore, *J. Fluid Mech.* 25 (1966) 321–330.
- M. Brocchini, A reasoned overview on Boussinesq-type models: the interplay between physics, mathematics and numerics, *Proc. R. Soc.* 469 (2013) 20130496.
- S. Glimsdal, G. Pedersen, C. Harbitz, F. Løvholt, Dispersion of tsunamis: does  
355 it really matter?, *Nat. Hazards Earth Syst. Sci.* 13 (2013) 1507–1526.
- F. Løvholt, G. Pedersen, C. Harbitz, S. Glimsdal, J. Kim, On the characteristics of landslide tsunamis, *Phil. Trans. R. Soc. A* 373 (2053) (2015) 20140376.
- J. Grue, E. N. Pelinovsky, D. Fructus, T. Talipova, C. Kharif, Formation of undular bores and solitary waves in the Strait of Malacca caused by the 26  
360 December 2004 Indian Ocean tsunami, *J. Geophys. Res.* 113 (2008) C05008.
- F. Løvholt, G. Pedersen, G. Gisler, Oceanic propagation of a potential tsunami from the La Palma Island, *J. Geophys. Res.* 113 (2008) C09026.
- J. Behrens, F. Dias, New computational methods in tsunami science, *Phil. Trans. R. Soc. A* 373 (2053) (2015) 20140382.
- 365 P. A. Madsen, O. R. Sørensen, A new form of the Boussinesq equations with improved linear dispersion characteristics. Part 2. A slowly-varying bathymetry, *Coastal Engineering* 18 (3) (1992) 183–204.
- O. Nwogu, Alternative form of Boussinesq equations for nearshore wave propagation, *Journal of waterway, port, coastal, and ocean engineering* 119 (6)  
370 (1993) 618–638.
- D. H. Peregrine, Long waves on a beach, *Journal of Fluid Mechanics* 27 (04) (1967) 815–827.

- A. B. Kennedy, Q. Chen, J. T. Kirby, R. A. Dalrymple, Boussinesq modeling of wave transformation, breaking, and run-up. Part I: 1D., J. Waterw., Port, Coast., Ocean Engrg. 126 (1) (2000) 39–47.
- 375 F. Løvholt, P. Lynett, G. K. Pedersen, Simulating run-up on steep slopes with operational Boussinesq models; capabilities, spurious effects and instabilities, Nonlin. Processes Geophys. 20 (2013) 379–395.
- H. A. Schäffer, P. A. Madsen, R. Deigaard, A Boussinesq model for waves breaking in shallow water, Coastal Engineering 20 (3) (1993) 185–202.
- 380 P. J. Lynett, Nearshore wave modeling with high-order Boussinesq-type equations, Journal of Waterway, Port, Coastal, and Ocean Engineering 132 (5) (2006) 348–357.
- M. Tissier, P. Bonneton, F. Marche, F. Chazel, D. Lannes, A new approach to handle wave breaking in fully non-linear Boussinesq models, Coastal Engineering 67 (2012) 54–66.
- 385 M. Matsuyama, M. Ikeno, T. Sakakiyama, T. Takeda, A study of tsunami wave fission in an undistorted experiment, Pure and Applied Geophysics 164 (2-3) (2007) 617–631.
- 390 K. Erduran, S. Ilic, V. Kutija, Hybrid finite-volume finite-difference scheme for the solution of Boussinesq equations, Int. J. for Num. Meth. in Fluids 49 (2005) 1213–1232.
- D.-H. Kim, P. Lynett, S. Socolofsky, A depth-integrated model for weakly dispersive, turbulent, and rotational flows, Ocean Modelling 27 (2009) 198–214.
- 395 F. Shi, J. T. Kirby, J. C. Harris, J. D. Geiman, S. T. Grilli, A high-order adaptive time-stepping TVD solver for Boussinesq modeling of breaking waves and coastal inundation, Ocean Modelling 43 (2012) 36–51.
- M. Tonelli, M. Petti, Hybrid finite volume–finite difference scheme for 2DH improved Boussinesq equations, Coastal Engineering 56 (5) (2009) 609–620.

- 400 P. J. Lynett, T. R. Wu, P. L. F. Liu, Modeling wave runup with depth-integrated equations, *Coastal Engineering* 46 (2) (2002) 89–107.
- G. Wei, J. T. Kirby, Time-dependent numerical code for extended Boussinesq equations, *Journal of Waterway, Port, Coastal, and Ocean Engineering* 121 (5) (1995) 251–261.
- 405 Clawpack Development Team, Clawpack software, URL <http://www.clawpack.org>, version 5.3.1, 2016.
- R. J. LeVeque, Wave propagation algorithms for multidimensional hyperbolic systems, *Journal of Computational Physics* 131 (2) (1997) 327–353.
- D. L. George, Augmented Riemann solvers for the shallow water equations over  
410 variable topography with steady states and inundation, *Journal of Computational Physics* 227 (6) (2008) 3089–3113.
- M. Tissier, P. Bonneton, F. Marche, F. Chazel, D. Lannes, Serre Green-Naghdi modelling of wave transformation breaking and run-up using a high-order finite-volume finite-difference scheme, *Coastal Engineering Proceedings* 1 (32)  
415 (2011) 13.
- D. Dutykh, T. Katsaounis, D. Mitsotakis, Finite volume methods for unidirectional dispersive wave models, *International Journal for Numerical Methods in Fluids* 71 (6) (2013) 717–736.
- R. J. LeVeque, Finite volume methods for hyperbolic problems, vol. 31, Cambridge university press, 2002.  
420
- Q. Chen, Fully nonlinear Boussinesq-type equations for waves and currents over porous beds, *J. of Eng. Mech., ASCE* 132 (2) (2006) 220–230.
- G. Wei, J. T. Kirby, S. T. Grilli, R. Subramanya, A fully nonlinear Boussinesq model for surface waves. Part 1. Highly nonlinear unsteady waves, *J. Fluid Mech.* 294 (1995) 71–92.  
425



- P. A. Madsen, O. Sørensen, H. Schäffer, Surf zone dynamics simulated by a Boussinesq type model. Part I. Model description and cross-shore motion of regular waves, *Coastal Engineering* 32 (4) (1997) 255–287.
- M. Briggs, C. Synolakis, U. Kanoglu, D. Green, Runup of solitary waves on a vertical wall, *Costal Hydraulics Laboratory*, URL <http://chl.erdc.usace.army.mil/chl.aspx?p=s&a=Projects;36>, 1995.
- C. E. Synolakis, The runup of solitary waves, *Journal of Fluid Mechanics* 185 (1987) 523–545.
- F. Løvholt, G. Pedersen, S. Glimsdal, Coupling of Dispersive Tsunami Propagation and Shallow Water Coastal, *Open Oceanography Journal* 4 (2010) 71–82.
- M. Antuono, L. Soldini, M. Brocchini, On the role of the Chezy frictional term near the shoreline, *Theoretical and Computational Fluid Dynamics* 26 (1-4) (2012) 105–116.
- T. B. Benjamin, J. L. Bona, J. J. Mahony, Model equations for long waves in nonlinear dispersive systems, *Philosophical Transactions of the Royal Society of London A: Mathematical, Physical and Engineering Sciences* 272 (1220) (1972) 47–78.

## Appendix A. Stability of the hybrid scheme

It is difficult to analyze the numerical stability for our full Boussinesq equations. To obtain some insight in the stability of the proposed hybrid numerical scheme, we thus consider a closely related, but simpler, equation, namely the linearized Benjamin-Bona-Mahony (BBM) equation (Benjamin et al. (1972))

$$u_t + cu_x = \frac{h^2}{6} u_{txx}, \quad (\text{A.1})$$

- where  $c = \sqrt{gh}$ . This equation describes weakly dispersive, uni-directional waves in constant depth. The equation replaces the momentum equation, whereas no separate continuity equation is involved.

Following the steps of section 2.1.2, we rearrange the equation (A.1) as

$$(I - D)(u_t + cu_x) + Du_x = 0, \quad (\text{A.2})$$

where  $D = \frac{h^2}{6} \partial_x^2$ . The first step of hybrid scheme for this equation is integration of the advection equation

$$u_t + cu_x = 0, \quad (\text{A.3})$$

by the finite volume method. Then the Runge-Kutta method is applied to,

$$(1 - D)u_t + cDu_x = 0. \quad (\text{A.4})$$

which is the counterpart to (7).

If we use the centered spatial difference approximation of  $O(\Delta x^2)$  accuracy  
 450 on a regular grid we may employ a standard von Neumann analysis where we  
 calculate the growth of an harmonic mode over a single time step. Expressing  
 the coefficients of the velocity array before the time step as  $u_j = e^{i\xi j \Delta x}$  we then  
 replace the coefficient of  $\mathbf{M}^q$ , defined in section 2.1.2, by  $M_j^q = U_j^q = g^q e^{i\xi j \Delta x}$ ,  
 where  $q$  is 1, 2, 3, 4 or +. Correspondingly, the coefficients of the  $\mathbf{S}^k$  array,  
 455 which contains auxiliary, nodal values for  $u_t$ , is expressed  $(S_j^k) = s^k e^{i\xi j \Delta x}$ .

The stability of the first step, (A.3), is assured by the standard CFL criterion

$$\frac{c\Delta t}{\Delta x} < 1.$$

If we instead solve the NLSW equations, as in BoussClaw,  $c$  must be replaced by  
 the nonlinear characteristic velocity, which may lead to a more strict criterion.  
 However, the method employed in the first step is not suited for a von Neumann  
 stability analysis and we thus apply this technique to the second step only.  
 Hence, we may put  $g^1$  to unity, but it is preferable to retain it in the calculations.  
 The Runge-Kutta scheme for time stepping, (8), may now be expressed as

$$g^2 = g^1 + \frac{\Delta t}{2} s^1, \quad g^3 = g^1 + \frac{\Delta t}{2} s^2, \quad g^4 = g^1 + \Delta t s^3, \quad (\text{A.5})$$

The discrete version of (A.4), which is the counterpart to (9) for the BBM  
 equation reads

$$S_j^k - \frac{h^2}{6} \frac{S_{j+1}^k - 2S_j^k + S_{j-1}^k}{\Delta x^2} = -\frac{ch^2}{6} \frac{U_{j+2}^k - 2U_{j+1}^k + 2U_{j-1}^k - U_{j-2}^k}{2\Delta x^3},$$

which, inserted the harmonic expressions, implies

$$s^k = i \frac{\gamma}{\Delta t} g^k, \quad \gamma = c \Delta t \frac{2 \sin(\xi \Delta x) (1 - \cos(\xi \Delta x))}{6 \Delta x^3 h^{-2} + 2 \Delta x (1 - \cos(\xi \Delta x))}, \quad (\text{A.6})$$

where the  $\Delta t$  factors are included for convenience. The assembling of the intermediate values in the Runge-Kutta procedure, (10), now yields

$$g^+ = g^1 + \frac{\Delta t}{6} [s^1 + 2s^2 + 2s^3 + s^4]. \quad (\text{A.7})$$

By combination of (A.5) and (A.6)  $s^k$  and  $g^k$ ,  $k = 1..4$  can be calculated successively and combined in (A.7) to provide the value of  $g^+$ ,

$$\begin{aligned} g^+(\gamma) &= \left(1 - \frac{1}{2}\gamma^2 + \frac{\gamma^4}{24} + \left(\frac{\gamma^3}{6} - \gamma\right)i\right) g^1 \\ |g^+(\gamma)|^2 &= \left(1 + \frac{1}{4}\gamma^4 + \frac{\gamma^8}{24^2} - \gamma^2 + \frac{\gamma^4}{12} - \frac{\gamma^6}{24} + \gamma^2 + \frac{\gamma^6}{36} - \frac{\gamma^4}{3}\right) |g^1|^2 \\ &= \left(1 - \frac{1}{72}\gamma^6 + \frac{1}{576}\gamma^8\right) |g^1|^2. \end{aligned}$$

Stability requires  $|g^+(\gamma)/g^1| < 1$  which is equivalent to  $|\gamma| < 2\sqrt{2}$ . Moreover, it is easily seen that  $\gamma < c\Delta t/\Delta x$ . Hence, a sufficient condition for stability of the second step of the hybrid scheme is

$$\frac{c\Delta t}{\Delta x} < 2\sqrt{2}.$$

This is more relaxed than the CFL condition for the advection equation (A.3). Therefore, if the CFL condition is satisfied in the advection equation, the fractional step is always stable with the suggested numerical scheme.

## Appendix B. Energy estimates and dissipation

### 460 Appendix B.1. Velocity field

To derive the energy estimates for the Boussinesq-type equations, we define the depth-averaged velocity as,

$$\bar{u} = \frac{1}{H} \int_{-h}^{\epsilon\eta} u dz.$$

Then the velocity  $u$  can be expressed as  $u = \bar{u} + \mu^2 u_1$  where

$$\int_{-h}^{\epsilon\eta} u_1 dz = 0. \quad (\text{B.1})$$

Then the kinematic boundary condition at the bottom and zero divergence implies

$$w = -h_x u - \bar{u}_x(z+h) + O(\mu^2).$$

### Appendix B.2. Energy integrals

The potential energy density per horizontal area is

$$V = \int_{-h}^{\epsilon\eta} g z dz = \frac{1}{2} \epsilon^2 g \eta^2 - \frac{1}{2} g h^2,$$

where the last term  $\frac{1}{2} g h^2$  is the equilibrium energy. The kinematic energy density has two contributions,

$$T = T_u + T_w; \quad T_u = \frac{1}{2} \epsilon^2 \int_{-h}^{\epsilon\eta} u^2 dz, \quad T_w = \frac{1}{2} \epsilon^2 \mu^2 \int_{-h}^{\epsilon\eta} w^2 dz.$$

For the horizontal part,  $T_u$  is

$$T_u = \frac{1}{2} \epsilon^2 \int_{-h}^{\epsilon\eta} u^2 dz = \frac{1}{2} \epsilon^2 \int_{-h}^{\epsilon\eta} \bar{u}^2 + 2\mu^2 \bar{u} u_1 + \mu^4 u_1^2 dz = \frac{1}{2} \epsilon^2 H \bar{u}^2 + O(\epsilon^2 \mu^4),$$

since  $\bar{u}$  is independent of  $z$  and by (B.1). Assuming  $\frac{1}{H} \int_{-h}^{\epsilon\eta} u^2 dz = \bar{u}^2$ , the vertical part is

$$\begin{aligned} T_u &= \frac{1}{2} \epsilon^2 \mu^2 \int_{-h}^{\epsilon\eta} h_x^2 u^2 + 2h_x u \bar{u}_x(z+h) + \bar{u}_x^2(z+h)^2 dz + O(\epsilon^2 \mu^4) \\ &= \frac{1}{2} \epsilon^2 \mu^2 H \left( h_x^2 \bar{u}^2 + H h_x \bar{u} \bar{u}_x + \frac{1}{3} H^2 \bar{u}_x^2 \right) + O(\epsilon^2 \mu^4). \end{aligned}$$

Thus the energy of a wave can be approximated as

$$E = \epsilon^2 (E_0 + \mu^2 E_1 + O(\mu^4))$$

where

$$\begin{aligned} E_0 &= \frac{1}{2} (g \eta^2 + H \bar{u}^2), \\ E_1 &= \frac{1}{6} H^3 \bar{u}_x^2 + \frac{1}{2} H^2 h_x \bar{u} \bar{u}_x + \frac{1}{2} H h_x^2 \bar{u}^2. \end{aligned}$$